GÜFBED/*GUSTIJ* (2020) 10 (4): 900-910 **Gümüşhane Üniversitesi Fen Bilimleri Enstitüsü Dergisi**
DOI: 10.17714/gumusfenbil.701475 Araştırma Makalesi / *Research Article*

Numerical Investigation of the Critical Current and Trapped Flux Properties of the HTS-PMG Arrangements

HTS-PMG Dizilimlerinin Kritik Akım ve Tuzaklanan Akı Özelliklerinin Nümerik Olarak İncelenmesi

Murat ABDİOĞLU*[1,2,a]

[1]*Department of Mathematics and Science Education, Faculty of Education, Bayburt University, 69000, Bayburt, Turkey.*
[2]*Department of Physics, Faculty of Science, Karadeniz Technical University, 61080, Trabzon, Turkey*

• Geliş tarihi / *Received*: 10.03.2020 • Düzeltilerek geliş tarihi / *Received in revised form*: 16.05.2020 • Kabul tarihi / *Accepted*: 17.07.2020

Abstract
The electromagnetic behaviour of the Maglev systems should be predicted to figure out the induced current and trapped flux distribution inside the high temperature superconductors (HTS) and thus to optimize the design of Maglev systems. In the present study, firstly the magnetic flux density distributions of single-PM and double-PM permanent magnetic guideways (PMGs) have been obtained numerically by using magneto-static solution in AC/DC Module in COMSOL Multiphysics package. Then the trapped magnetic flux and induced current inside the HTS have been determined under the non-uniform magnetic field via the Partial Differential Equation (PDE) Mode in COMSOL by using H-formulation. Obtained numerical results in this study showed that different PMG configurations have various magnetic field characteristic and this situation can improve the magnetic and supercurrent properties of the HTS in Maglev system.

Keywords: Bulk Superconductors, Electromagnetic Simulation, Permanent Magnetic Guideway

Öz
Yüksek sıcaklık süperiletkenleri (HTS) içinde indüklenen akım ve tuzaklanan akı dağılımının belirlenmesi ve böylece Maglev sistemlerinin tasarımının optimize edilmesi için Maglev sistemlerinin elektromanyetik davranışı belirlenmelidir. Bu çalışmada, ilk olarak COMSOL Multiphysics paket programının AC/DC Modülündeki manyeto-statik çözüm kullanılarak tek-PM ve çift-PM manyetik kılavuzlama yollarının (PMG) manyetik akı yoğunluğu dağılımlarını sayısal olarak elde edildi. Daha sonra H-formülasyonu kullanarak COMSOL'daki Kısmi Diferansiyel Denklem (PDE) modu ile homojen olmayan manyetik alan altında HTS içindeki tuzaklanan manyetik akı ve indüklenen akı belirlendi. Bu çalışmada elde edilen sayısal sonuçlar, farklı PMG konfigürasyonlarının çeşitli manyetik alan karakteristiklerine sahip olduğunu ve bu durumun Maglev sistemindeki HTS'nin manyetik ve süper akım özelliklerini iyileştirebileceğini göstermiştir.

***Anahtar kelimeler**: Külçe Süperiletkenler, Elektromanyetik Simulasyon, Manyetik Kılavuzlama Yolu*

*[a] Murat ABDİOĞLU; muratabdioglu61@gmail.com, Tel: (0458) 2111153, orcid.org/0000-0002-5497-0817

1. Introduction

The relative motion between the high temperature superconductor (HTS) and the permanent magnet (PM) creates a repulsive or attractive force which is called as levitation force. This levitation force stems from the induced supercurrents inside the HTS due to the inhomogeneous magnetic field which HTS exposures. This unique property of superconductors is used to develop magnetically levitated transportation (Maglev) systems (Deng et al., 2017; Kusada et al., 2007; Sotelo et al., 2015; Ozturk et al., 2019; Abdioglu et al., 2015), flywheel energy storage systems (Werfel et al., 2012; Basaran and Sivrioglu, 2017), superconducting motors (Hull and Strasic, 2010; Masson and Luongo, 2005; 10_Kovalev et al., 2016) and magnetic resonance imaging (MRI) devices (Minervini et al., 2018; Yamamoto et al., 2014), etc. The studies on Maglev systems have increased since the development of first man–loaded Maglev vehicle in 2002 by the group of Southwest Jiaotong University in China (Wang et al., 2002). Researchers have focused on improving the magnetic levitation and guidance forces of Maglev systems for enhancing the loading capacity and movement stability, respectively. Many studies have been carried out until now to improve the practical applicability potential of Maglev systems via experimental (Deng et al., 2017; Kusada et al., 2007; Sotelo et al., 2015; Abdioglu et al., 2015; Guner et al., 2019), analytical (Ozturk et al., 2019; Ainslie and Fujishiro 2015) and numerical (Ainslie and Fujishiro 2015; Zhang and Coombs, 2012; Ozturk et al., 2012) methods. The electromagnetic behaviour of the above systems should be predicted to figure out the induced current and trapped flux distribution inside the HTS and thus to optimize the design of Maglev systems.

There are several analytical and numerical methods in literature which are used for predicting the electromagnetic characteristics of Maglev systems. The analytical methods are useful for simple geometries and uniform magnetic field conditions, while the numerical methods are effective in more complicated geometries (Ozturk et al., 2012). Navau et al. have discussed different analytical and numerical solutions of the critical state model (CSM) and made a detailed review on the main characteristics and parameters of the magnetization loops and levitation forces (Navau et. al 2013). The finite element method (FEM) based on CSM is frequently used to calculate the levitation force, magnetization and trapped flux. Various formulations are used in FEM such as A-V formulation (Sotelo et al., 2009; Dias et al., 2010; Ruiz-Alonso et al., 2004), T-Ω formulation (Zheng and Yang 2007), E-formulation and H-formulation (Ozturk et al., 2012; Sass et al., 2015; Patel et al., 2015; Quéval et al., 2018; Hong et al., 2006). Quéval et al. have reported different formulations used in finite element models (Quéval et al., 2018).

The studies in literature, generally uses single-PM rather than double-PM (meanly PMG) and there is no detailed study on the critical current and trapped flux densities of the superconductor by using single and double-PM arrangements. In the present study, firstly magnetic flux density distributions of two different PMGs have been obtained numerically by using magneto-static solution in AC/DC Module in COMSOL Multiphysics package. Then the trapped magnetic flux and induced current inside the HTS under the non-uniform magnetic field have been determined via the Partial Differential Equation (PDE) Mode in COMSOL by using H-formulation (Ozturk et al., 2012; Hong et al., 2006).

2. Numerical Scheme

The magnetic field distribution data of PMG is obtained by numerical modelling via magnetostatic solution in COMSOL Multiphysics. Eq. (1) and Eq. (2) are used, respectively, to define the physical parameters (B_z and B_r) of magnetic medium and air. Where, B, H, M and μ_0 represent the magnetic flux density, magnetic field, magnetization and magnetic permeability of the free space, respectively.

$$\vec{B} = \mu_0 \vec{H} + \mu_0 \vec{M} \quad (1)$$

$$\vec{B} = \mu_0 \vec{H} \quad (2)$$

The numerical method in this study to predict the electromagnetic characteristics of Maglev system is based on solving the Maxwell equations in Partial Differential Equation Mode by using the H-formulation in COMSOL Multiphysics 3.5a which based on the finite element method. The Maxwell equations used in this study are given as:

$$\nabla \times \vec{E} = -\mu \frac{\partial \vec{H}}{\partial t} \quad (3)$$

$$\vec{J} = \nabla \times \vec{H} \quad (4)$$

$$\vec{E} = \rho \vec{J} \quad (5)$$

where $\vec{E}$ is electrical field, $\vec{J}$ is critical current density, ρ is resistivity and $\mu = \mu_0\mu_r$ and relative permeability, $\mu_r$is taken as 1 for HTS bulks.

The numerical scheme is based on dividing the 2D space into three subdomains as superconducting region, dielectric region (air) and magnetization region (Ozturk et al., 2012; Hong et al., 2006). Two partial differential equations (PDEs) are solved in this numerical scheme by using the general form PDE mode in COMSOL for the dependent variables of H_r and H_z which are the magnetic field components in *r*- and *z*-directions, respectively. The critical current density J_{sc_φ} and electrical field E_{sc_φ} of the HTS are calculated in the superconducting region and these are perpendicular to the *r*-*z* plane. By using Faraday's and Ampere's law in Eqs. (3) and (4), respectively, one can obtain the following equation for cylindrical symmetry:

$$-\hat{r}\frac{\partial E_{sc\_\varphi}}{\partial z} + \hat{z}\frac{1}{r}\frac{\partial\left(rE_{sc\_\varphi}\right)}{\partial r} = -\mu_0\mu_r\left(\hat{r}\frac{\partial H_r}{\partial t} + \hat{z}\frac{\partial H_z}{\partial t}\right) \quad (6)$$

$$J_{sc\_\varphi} = \frac{\partial H_r}{\partial z} - \frac{\partial H_z}{\partial r} \quad (7)$$

Where J_{sc_φ} indicates the φ component of superconducting current density induced inside the HTS, flowing azimuthally as perpendicular to the *r*-*z* plane. The electrical behaviour of superconductors has nonlinear character due to including the flux pinning centres. Therefore, according the E-J power law, the electric field of the HTS can be described as

$$E_{sc\_\varphi} = E_0\left(\frac{J_{sc\_\varphi}}{J_c(B)}\right)^{\alpha} \quad (8)$$

where $E_0 = 1\times10^{-4}\ V/m$, $J_c(B)$ is the magnetic field dependent critical current density of the HTS and α=21 for type-II superconductors (Yamasaki and Mawatari, 2000). On the other hand, for the dielectric region (air), the electrical behaviour can be described by linear Ohm law as

$$E_{sc\_\varphi} = \rho J_{sc\_\varphi} \quad (9)$$

where ρ is the resistivity of dielectric region. The critical current density of HTS and the magnetic flux density are given by

$$J_c(B) = \frac{J_{c0}}{\left(1+\frac{B}{B_0}\right)^{\beta}} \quad (10)$$

$$B = \mu_0\mu_r\sqrt{H_r^2 + H_z^2} \quad (11)$$

where, B_0 and β are material dependent constants, and J_{c0} is the magnitude of the critical current density at the temperature of 77 K when the local field is zero. In this study, modified Kim-like model was used to determine $J_c(B)$ value dependent on the magnetic field (Zou et al., 2015; Zhai et al., 2013). Vertical (H_z) and lateral (H_r) components of the magnetic fields are obtained as follows by inserting the Eqs. (7)–(10) into (6):

$$\partial\left(rE_0\left(\frac{(\partial H_z/\partial r)-(\partial H_r/\partial z)}{J_c(B)}\right)^{\alpha}\right)/\partial z = -\mu_0\mu_r\, r\frac{\partial H_r}{\partial t}, \quad (12)$$

$$-\partial\left(rE_0\left(\frac{(\partial H_z/\partial r)-(\partial H_r/\partial z)}{J_c(B)}\right)^{\alpha}\right)/\partial r = -\mu_0\mu_r\, r\frac{\partial H_z}{\partial t}, \quad (13)$$

3. Results and Discussions

In this study, the magnetic flux density distribution, trapped magnetic flux and supercurrent density between the HTS and two different magnetic field sources were modelled. One of these field sources is named as single–PM (see Figure 1b) and the other one is named as double-PM (see Figure 1a). The lateral (B_r) magnetic flux density distributions of two different PMGs are given in Figure 1 at 2 mm, 5 mm and 10 mm away from the PMG upper surface. In modelling, the magnetization value of each PM was taken as 11324904 A/m. One can see from Figure 1 that both at the upper side and right side of the PMGs, the peak values of magnetic flux density distribution curves decrease with increasing distance from the PMG. In addition, one can see that the maximum B_r value was obtained as 0.48 T at 2 mm away from the upper surface and 0.55 T at 2 mm away from the right side, for double–PM as consistent with the studies in literature (Ozturk et al., 2019). The bigger B_r value at the right side can be attributed to the condensed magnetic flux density on the right surface because of the head–to–head directed PMs. It is also seen from Figure 1 that the maximum B_r values at the upper surface of single–PM is slightly bigger than that of double–PM since the head–to–head directed PMs decrease the magnetic flux distribution on the upper surface of double–PM.

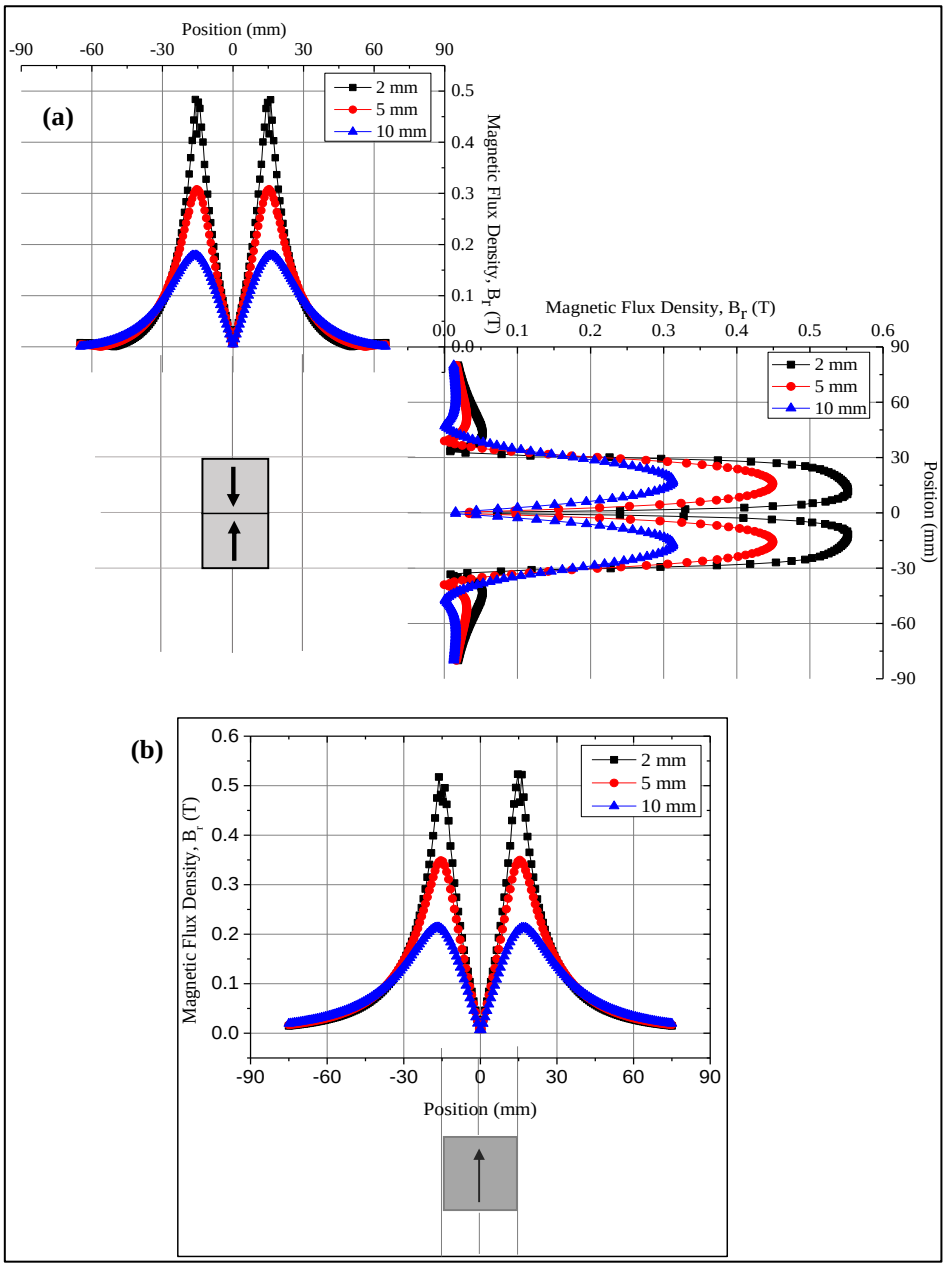

Figure 1. Lateral (B_r) magnetic flux density distributions of (a) double-PM and (b) single-PM PMGs obtained at 2 mm, 5 mm and 10 mm away from the PMG surface by using the magnetostatic solution.

Figure 2 shows the vertical (B_z) magnetic flux density distributions of two different PMGs at 2 mm, 5 mm and 10 mm away from the PMG surface. It is seen from this figure that the maximum B_z value was obtained as 0.36 T at 2 mm away from the upper side and 1.08 T at 2 mm away from the right side, for double–PM. This is attributed to the condensed magnetic flux density on the right surface because of the head–to–head directed PMs, as consistent with Figure 1. In addition, the maximum B_z value was obtained as 0.45 T at 2 mm away from the upper surface of single–PM which is bigger than that of the double–PM. The bigger B_r and B_z values at the right sides of double-PM are bigger than that of the single-PM as seen in Figure 1 and Figure 2 is an important result in point of supercurrents which can be induced inside the superconductors.

The symbols, descriptions and the values of the constants which are used in numerical calculations of this study are given in Table 1. Figure 3 shows the screenshot and J_{sc_ϕ} current density distribution of one half of the HTS sample with dimensions of 64 mm x 14 mm and single-PM. In the Figure 3, surface plot shows induced supercurrents while arrows show the magnetic field. The magnetic field of PM was supplied by a non-uniform external field of a normal conductor coil carrying current density as $J(t) = \mathrm{J}_0 \sin(\omega t)$ for $\omega t = \pi$ in axially symmetric geometry. The parameters which are used in this study are given in Table 1.

The supercurrents occur inside the HTS gradually depending on time as can be seen from different tones of colors in Figure 3a-c. In addition, the critical current density gets smaller as going to the inner regions of the HTS.

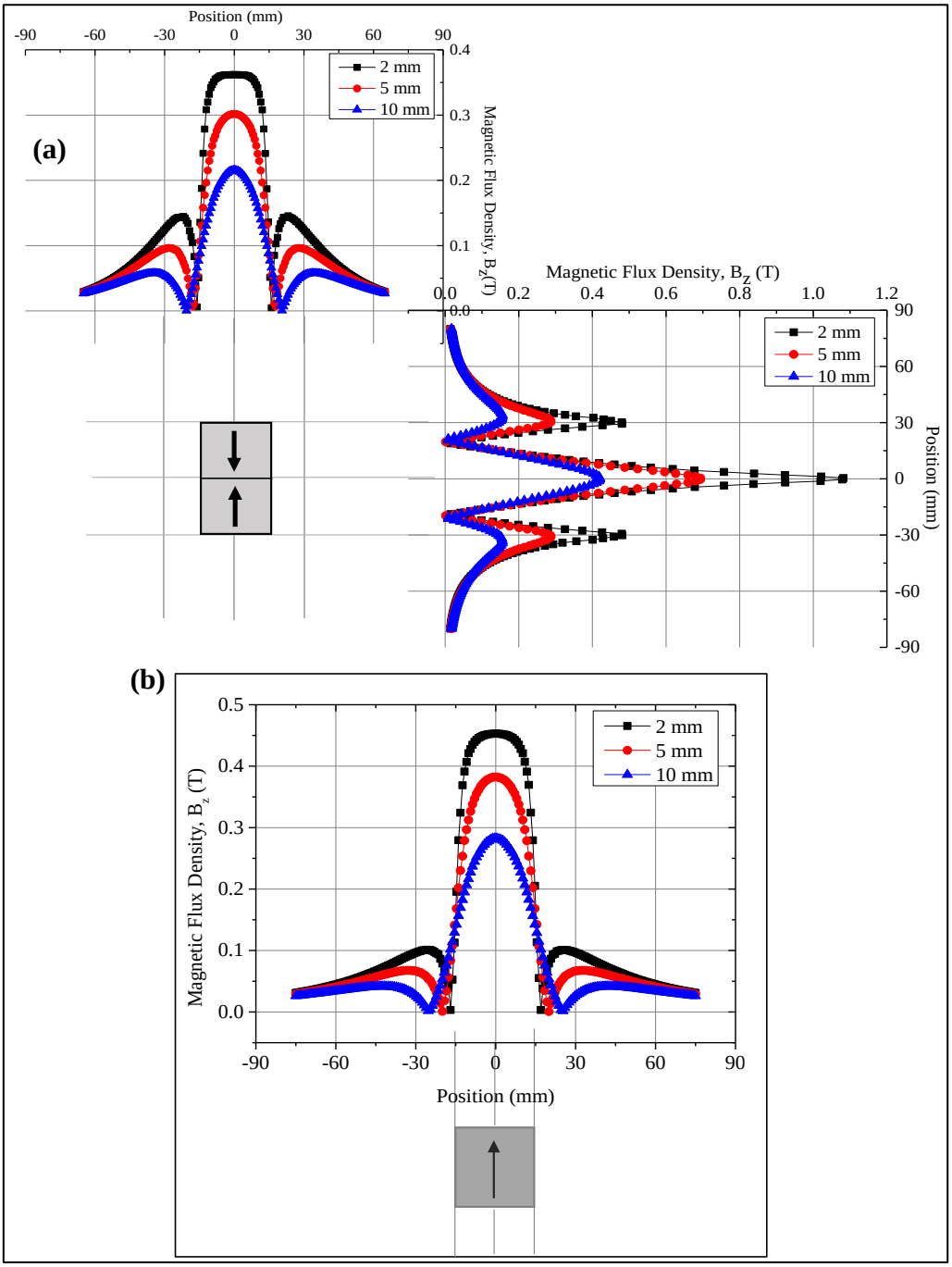

Figure 2. Vertical (B_z) magnetic flux density distributions of (a) double-PM and (b) single-PM PMGs obtained at 2 mm, 5 mm and 10 mm away from the PMG surface by using the magnetostatic solution

The symbols, descriptions and the values of the constants which are used in numerical calculations of this study are given in Table 1. Figure 3 shows the screenshot and J_{sc_ϕ} current density distribution of one half of the HTS sample with dimensions of 64 mm x 14 mm and single-PM. In the Figure 3, surface plot shows induced supercurrents while arrows show the magnetic field. The magnetic field of PM was supplied by a non-uniform external field of a normal conductor coil carrying current density as $J(t) = \mathrm{J}_0 \sin(\omega t)$ for $\omega t = \pi$ in axially symmetric geometry. The parameters which are used in this study are given in Table 1. The supercurrents occur inside the HTS gradually depending on time as can be seen from different tones of colors in Figure 3a-c. In addition, the critical current density gets smaller as going to the inner regions of the HTS.

Table 1. Constants used in modelling

Symbol	Description	Value
ρ_{metal}	Resistivity of wire (Ω m)	1
J_0	Peak wire current (A m^{-2})	7.98×10^{7}
μ_0	Permeability of vacuum (H m^{-1})	$4\pi\times10^{-7}$
α	Parameter for resistivity model	21
ρ_{air}	Resistivity of air (Ω m)	1.00×10^{6}
ω	Time constant for applied current (s)	1000 π
T	Temperature (K)	77
E_0	Parameter for E-J law (V m^{-1})	1.00×10^{-4}
J_{c0}	Constant parameter for J_c (A m^{-2})	3.62×10^{8}
B_0	Constant parameter for B (T)	6.85×10^{-2}
m	Constant parameter for m (A m^2)	4.50×10^{-1}

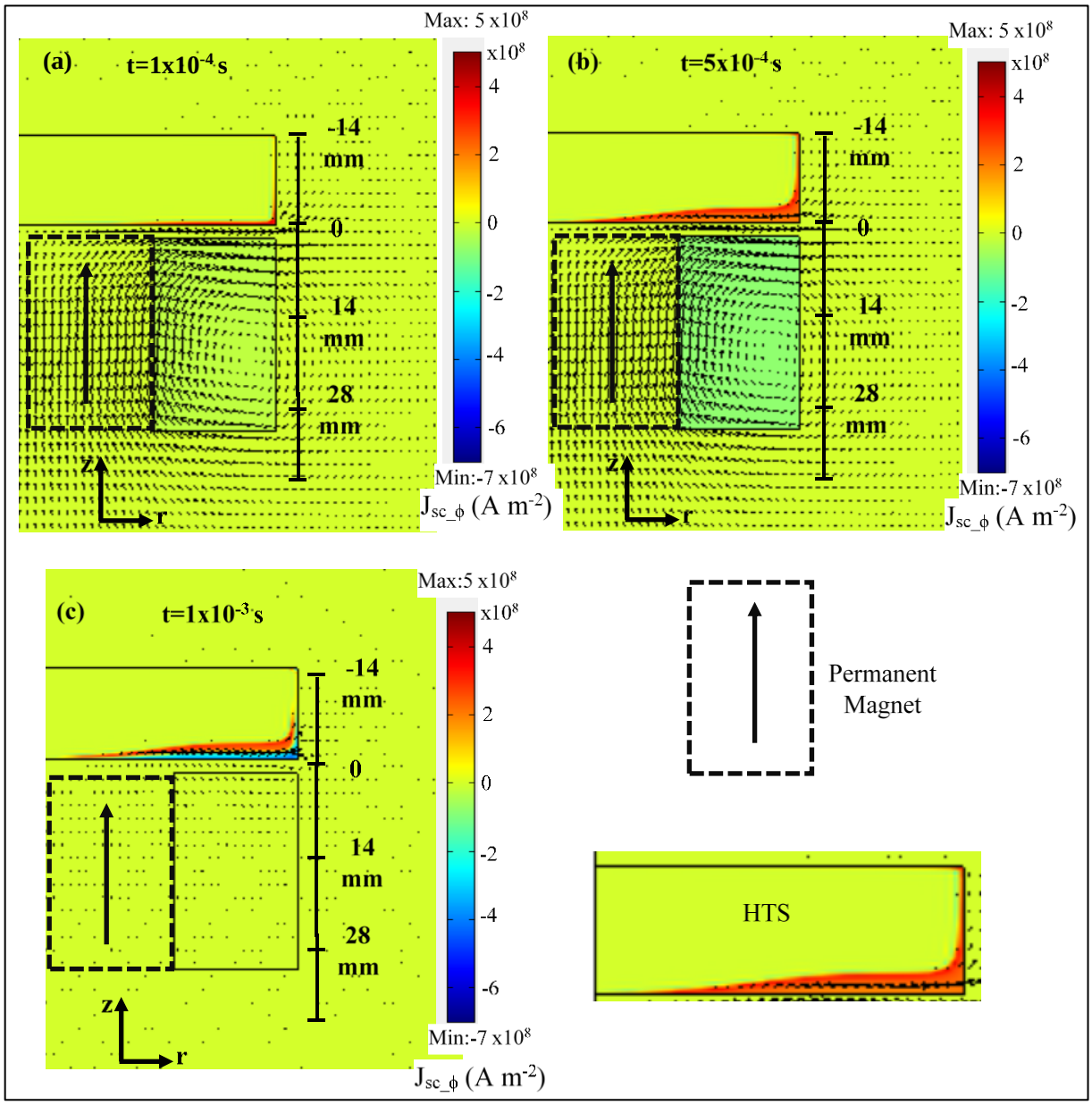

Figure 3. Screenshot of the HTS and single-PM and Jsc_ϕ current density distribution of the HTS sample with 64 mm x 14 mm (3D size of the sample is 64x34x14 mm3) at different times of (a) t=1□10-4s, (b) t=5□10-4s and (c) t=1□10-3s. Surface plot shows induced supercurrents while arrows show the magnetic field. The arrow on the PM indicates the magnetization direction of the PM.

The z-component of the trapped magnetic flux density B_z distribution on the superconductor at different distances from the sample surface is shown in Figure 4 for single-PM. It can be seen from this figure that the trapped magnetic field increases with decreasing distance from the sample surface. It is also seen that maximum trapped magnetic field at the minimum gap of 1 mm was obtained as 0.06 T.

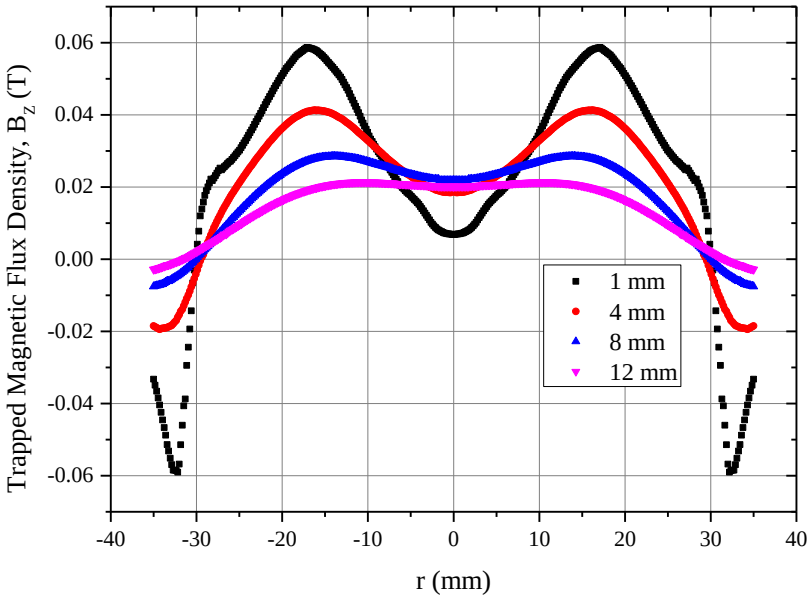

Figure 4. z-component of the trapped magnetic flux distribution, B_z, on the superconductor at different distances from the sample surface, with single-PM.

Figure 5 shows the J_{sc_ϕ} current density distribution at different distances inside the HTS surface as a function of lateral distance, with single-PM. As can be seen from the figure that the current density goes to negative values at the distance of 0.15 mm inside the HTS surface, indicating the flowing currents in opposite direction in regard to that of at the deeper distances below the surface and the maximum current density was obtained as -4.5×10^{8} Am^{-2}. One can see from Figure 5 that maximum current density was obtained as 4×10^{8} Am^{-2} at the distance of 3.5 mm inside the HTS surface and at the lateral distance of 30 mm, meanly near the edge of the HTS. However, one can see that at the lateral distances less than 30 mm, the current density obtained at 2.5 mm is bigger than that of 3.5 mm.

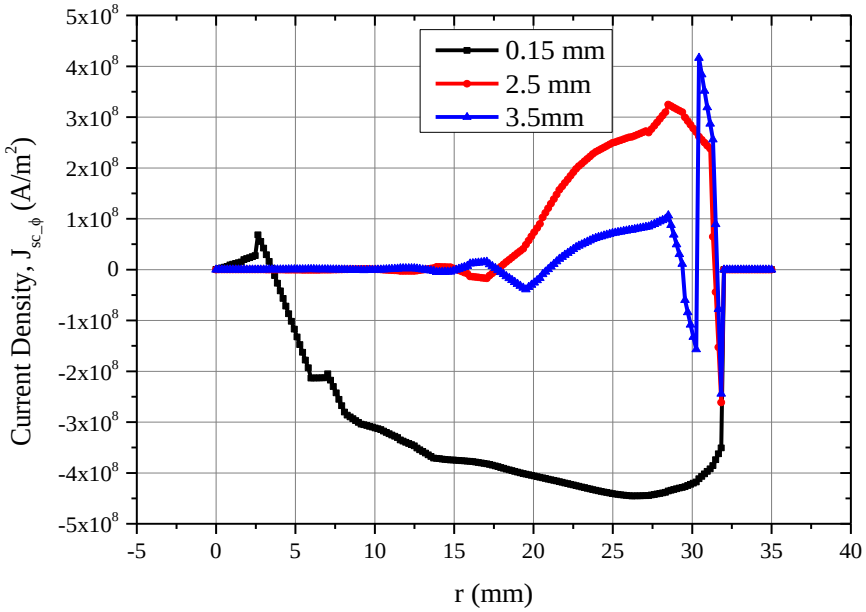

Figure 5. J_{sc_ϕ} current density distribution at different distances inside the sample surface as a function of lateral distance, with single-PM.

The screenshot and J_{sc_ϕ} current density distribution of one half (width was taken as 7 mm in vertical direction) of the HTS sample with dimensions of 64 mm x 14 mm and screenshot of the HTS and double-PM are shown in Figure 6. The gradually forming of supercurrents into the sample is clear in this figure, depending on solution time. It is also seen from Figure 6b-c that the current density distribution shows antisymmetric behavior in the above and below parts of the HTS and it is nearly zero at the center.

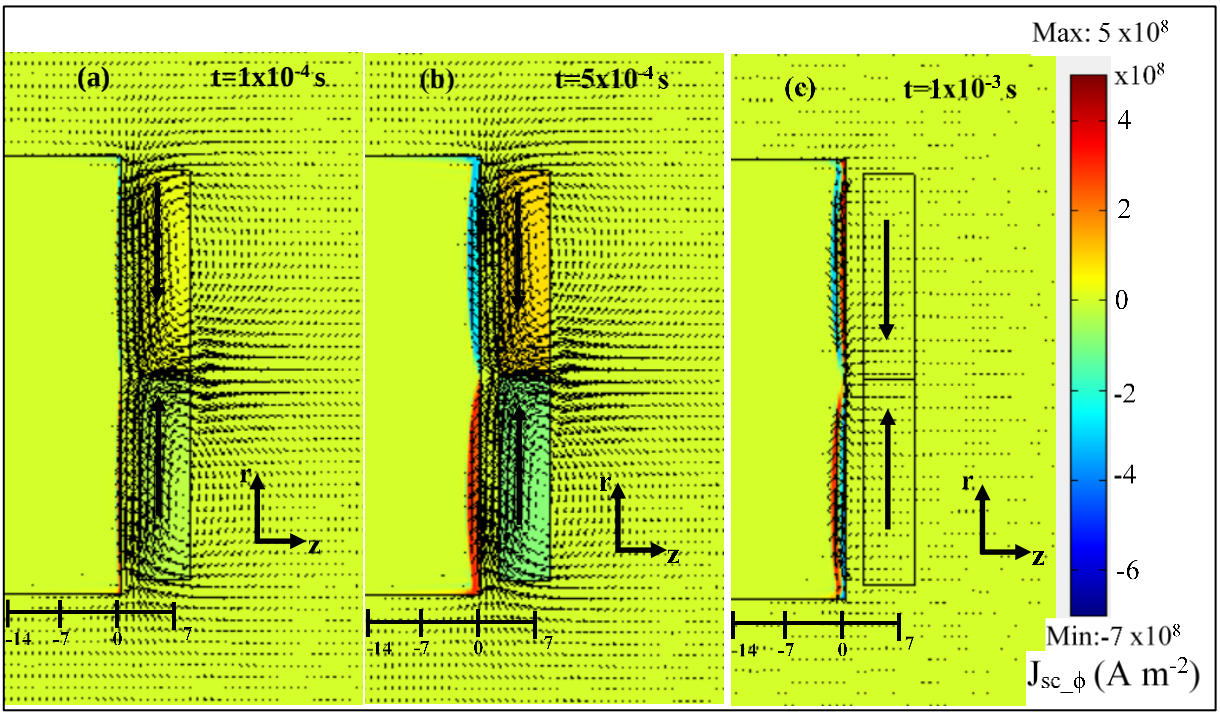

Figure 6. Screenshot of the HTS and double-PM and J_{sc_ϕ} current density distribution of the HTS sample with 64 mm x 14 mm (3D size of the sample is 64x34x14 mm^3) at different times of (a) t=1×10^{-4}s, (b) t=5×10^{-4}s and (c) t=1×10^{-3}s.

The z-component of the trapped magnetic flux distribution B_z on the superconductor at different distances from the sample surface is shown in Figure 7 with double-PM. As can be seen from this figure that the trapped flux decreases with increasing distance from the sample surface. Additionally, one can see that the trapped flux reaches maximum value at the lateral distance of 0 mm, meanly the center of the HTS, except at the distance of 1 mm from the surface. At this distance, the trapped flux curve shows a valley behavior due to the magnetic potential wall (Moon, 1994).

Figure 8 shows the J_{sc_ϕ} current density for different distances inside the HTS surface with double-PM as a function of lateral distance. As can be seen from the figure, the current density curves are symmetrical with respect to both the horizontal and vertical axes. This a result of the identical magnetic field properties of the permanent magnets and homogenous bulk structure of the HTS. The maximum current density at the minimum distance inside the surface of 0.15 mm was observed as 4.2×10^8 Am^{-2}. This current density value is compatible with the values in literature (Ozturk et al., 2012; Zhai et al., 2013).

The maximum value of current density inside the HTS sample was obtained at the lateral range of 20-30 mm with single-PM, while it was obtained at the lateral range of 0-30 mm for double-PM. In addition, the current density of double-PM shows a homogenous and stable distribution depending on lateral distance and depth from the surface while that of single-PM has a current density with different signs and changing values at lateral range of 0-30 mm. This situation indicates that the double-PM arrangements can have an advantage to the single-PM in levitation force performances of Maglev systems because of levitation force depends on the homogeny current density distribution and radius of shielding current in the bulk sample.

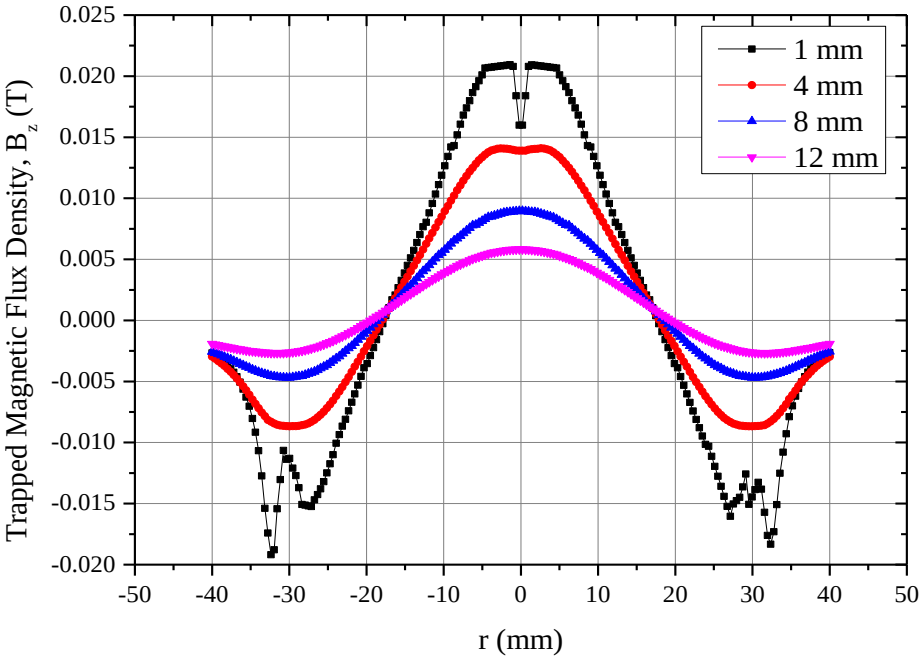

Figure 7. z-component of the trapped magnetic flux distribution B_z, with double-PM, on the superconductor at different distances from the sample surface.

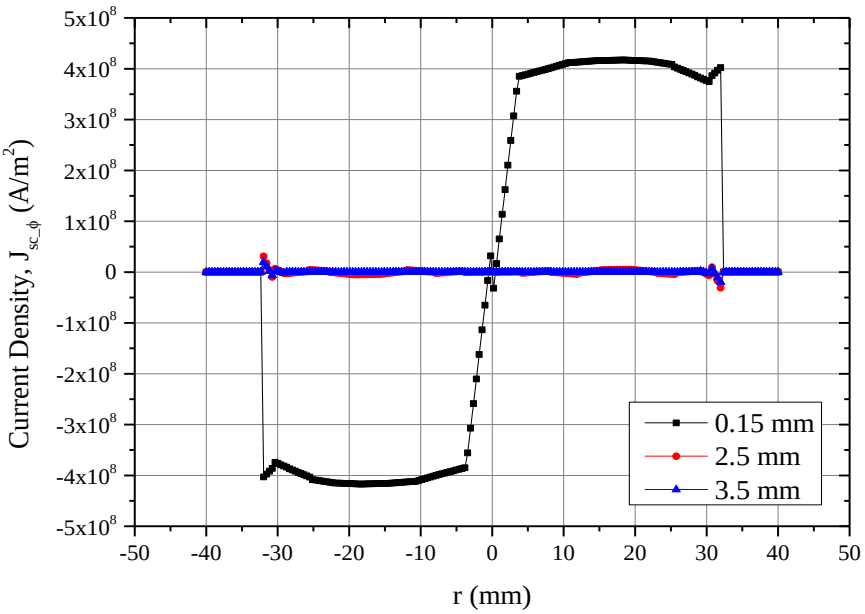

Figure 8. J_{sc_ϕ} current density inside the sample at different distances inside the sample surface with double-PM as a function of radius.

4. Conclusions

In this study, we have obtained magnetic flux density distributions of two different PMGs of single-PM and double-PM numerically by using magneto-static solution in AC/DC Module in COMSOL Multiphysics package. Then we have determined the trapped magnetic flux and induced current inside the HTS under the non-uniform magnetic field via the Partial Differential Equation (PDE) Mode in COMSOL by using H-formulation. The maximum current density was obtained as -4.5×10^8 Am^{-2} and 4.2×10^8 Am^{-2} at the distance of 0.15 mm inside the HTS surface by using single-PM and double-PM, respectively. The maximum value of current density inside the HTS sample was obtained at the lateral range of 20-30 mm with single-PM, while it was obtained at the lateral range of 0-30 mm for double-PM. In addition, the current density distribution of double-PM arrangement showed a very homogenous behavior while it had different signs and changing values at lateral range of 0-30 mm. It can be concluded from this study that different

PMG configurations have various magnetic field characteristic and this situation can improve the magnetic and supercurrent properties of the HTS in Maglev system.

Acknowledgement

This work was supported by the Scientific and Technological Research Council of Turkey (TÜBİTAK) with project numbers of 112T090 and 118F426. The author also would like to thank to Prof. Kemal OZTURK for his kind scientific contribution to this work.

References

Abdioglu, M., Ozturk, K., Gedikli, H., Ekici, M. and Cansiz, A. 2015. Levitation and Guidance Force Efficiencies of Bulk YBCO for Different Permanent Magnetic Guideways. Journal of Alloys and Compounds. 630, 260–265.

Ainslie, M. D. and Fujishiro, H. 2015. Modelling of Bulk Superconductor Magnetization. Superconductor Science and Technology, 28, 053002 (20pp).

Basaran, S. and Sivrioglu, S. 2017. Radial Stiffness Improvement of a Flywheel System Using Multi-Surface Superconducting Levitation. Superconductor Science and Technology, 30, 035008 (12pp).

Deng, Z., Zhang, W., Zheng, J., Wang, B., Ren, Y., Zheng, X. and Zhang, J., 2017. A High-Temperature Superconducting Maglev-Evacuated Tube Transport (HTS Maglev-ETT) Test System. IEEE Transactions on Applied Superconductivity, 27 (6) 3602008 (8pp).

Dias, D. H. N., Motta, E. S., Sotelo, G.G. and de Andrade Jr., R. 2010. Experimental Validation of Field Cooling Simulations for Linear Superconducting Magnetic Bearings. Superconductor Science and Technology, 23, 075013 (6pp).

Güner, S. B., Savaşkan, B., Öztürk, K., Çelik, Ş., Aksoy, C., Karaboğa, F., Taylan Koparan, E. and Yanmaz, E. 2019. Investigation on Superconducting and Magnetic Levitation Force Behaviour of Excess Mg Doped-Bulk MgB2 Superconductors. Cryogenics 101, 131–136.

Hong, Z., Campbell, A. M. and Coombs, T. A. 2006. Numerical Solution of Critical State in Superconductivity by Finite Element Software. Superconductor Science and Technology, 19, 1246–1252.

Hull, J. R. and Strasik, M. 2010. Concepts for Using Trapped-Flux Bulk High-Temperature Superconductor in Motors and Generators. Superconductor Science and Technology, 23, 124005 (7pp).

Kovalev, K. L., Verzhbitsky, L. G., Kozub, S. S., Penkin, V. T., Larionov, A. E., Modestov, K. A., Ivanov, N. S., Tulinova, E. E. and Dubensky, A.A. 2016. Brushless Superconducting Synchronous Generator with Claw-Shaped Poles and Permanent Magnets. IEEE Transactions on Applied Superconductivity., 26 (3), 5203204 (4pp).

Kusada, S., Igarashi, M., Nemoto, K., Okutomi, T., Hirano, S., Kuwano, K., Tominaga, T., Terai, M., Kuriyama, T., Tasaki, K., Tosaka, T., Marukawa, K., Hanai, S., Yamashita, T., Yanase, Y., Nakao, H. and Yamaji, M., 2007. The Project Overview of the HTS Magnet for Superconducting Maglev. IEEE Transactions on Applied Superconductivity, 17 (2), 2111-2116.

Masson, P. J. and Luongo, C. A. 2005. High Power Density Superconducting Motor for All-Electric Aircraft Propulsion. IEEE Transactions on Applied Superconductivity, 15 (2), 2226-2229.

Minervini, J., Parizh, M. and Schippers, M. 2018. Recent Advances in Superconducting Magnets for MRI and Hadron Radiotherapy: An Introduction to 'FOCUS on Superconducting Magnets for Hadron Therapy and MRI' Superconductor Science and Technology. 31, 030301 (4pp).

Moon, F. C. 1994. Superconducting Levitation, New York: Wiley.

Navau, C., Del-Valle, N. and Sanchez, A. 2013. Macroscopic Modeling of Magnetization and Levitation of Hard Type-II Superconductors: The Critical-State Model. IEEE Transactions on Applied Superconductivity, 23 (1), 8201023 (23 pp).

Ozturk, K., Guner, S. B., Abdioglu, M., Demirci, M., Celik, S. and Cansiz, A. 2019. An Analysis on the Relation Between the Seed Distance and Vertical Levitation Force for the Multi-Seeded YBCO Using the Modified Advanced Frozen Image (MAFI) and Experimental Methods. Journal of Alloys and Compounds, 805, 1208–1216.

Ozturk, K., Patel, A. and Glowacki, B. A. 2012. A Numerical Study to Investigate Magnetization, Current Density and Trapped Field Properties of Doped-Sm123 Bulk Superconductor Under Different Magnetic Fields. Physica Status Solidi A, 209 (12), 2558–2564.

Patel, A., Hopkins, S. C., Baskys, A., Kalitka, V., Molodyk, A. and Glowacki, B. A. 2015. Magnetic Levitation Using High Temperature

Superconducting Pancake Coils as Composite Bulk Cylinders. Superconductor Science and Technology, 28, 115007 (10pp).

Quéval, L., Liu, K., Yang, W., Zermeño, V. M. R. and Ma, G. 2018. Superconducting magnetic Bearings Simulation Using an H-formulation Finite Element Model. Superconductor Science and Technology, 31, 084001 (14pp).

Ruiz-Alonso, D., Coombs, T. A. and Campbell, A. M. 2004. Numerical Analysis of High-Temperature Superconductors With the Critical-State Model. IEEE Transactions on Applied Superconductivity, 14 (4), 2053-2063.

Sass, F., Sotelo, G. G., de Andrade Jr., R. and Sirois, F. 2015. H-formulation for simulating levitation forces acting on HTS Bulks and Stacks of 2G Coated Conductors. Superconductor Science and Technology, 28, 125012 (12pp).

Sotelo, G. G., de Andrade Jr., R. and Ferreira, A. C. 2009. Test and Simulation of Superconducting Magnetic Bearings. IEEE Transactions on Applied Superconductivity, 19 (3), 2083-2086.

Sotelo, G. G., R. de Oliveira, A. H., Costa, F. S., Dias, D. H. N., de Andrade, Jr, R. and Stephan, R. M. 2015. A Full Scale Superconducting Magnetic Levitation (MagLev) Vehicle Operational Line. IEEE Transactions on Applied Superconductivity, 25 (3) 3601005 (5pp).

Wang, J., Wang, S., Zeng, Y., Huang, H., Luo, F., Xu, Z., Tang, Q., Lin, G., Zhang, C., Ren, Z., Zhao, G., Zhu, D., Wang, S., Jiang, H., Zhu, M., Deng, C., Hu, P., Li, C., Liu, F., Lian, J., Wang, X., Wang, L., Shen, X. and Dong, X. 2002. The First Man-Loading High Temperature Superconducting Maglev Test Vehicle in the World. Physica C 378–381, 809–814.

Werfel, F. N., Floegel-Delor, U., Rothfeld, R., Riedel, T., Goebel, B., Wippich, D. and Schirrmeister, P. 2012. Superconductor Bearings, Flywheels and Transportation. Superconductor Science and Technology, 25, 014007 (16pp).

Yamamoto, S., Konii, K., Tanabe, H., Yokoyama, S., Matsuda, T. and Yamada, T. 2014. Super-Stable Superconducting MRI Magnet Operating for 25 Years. IEEE Transactions on Applied Superconductivity, 24 (3), 4400604 (4pp).

Yamasaki, H. and Mawatari, Y. 2000. Current–voltage characteristics and flux creep in melt-textured YBa2Cu3O7-x. Superconductor Science and Technology, 13, 202–208.

Zhai, W. Shi, Y. H., Durrell, J. H., Dennis, A. R., Rutter, N. A., Troughton, S. C., Speller, S. C. and Cardwell, D. A. 2013. The Processing and Properties of Single Grain Y–Ba–Cu–O Fabricated From Graded Precursor Powders. Superconductor Science and Technology, 26, 125021 (11pp).

Zhang, M. and Coombs, T. A. 2012. 3D Modeling of High-Tc Superconductors by Finite Element Software. Superconductor Science and Technology, 25, 015009 (7pp).

Zheng, X. and Yang, Y. 2007. Transition Cooling Height of High-Temperature Superconductor Levitation System. IEEE Transactions on Applied Superconductivity, 17 (4), 3862-3866.

Zou, J., Ainslie, M. D., Hu, D., Zhai, W., Devendra Kumar, N., Durrell, J. H., Shi, Y. H. and Cardwell, D. A. 2015. Numerical Simulation and Analysis of Single Grain YBCO Processed From Graded Precursor Powders. Superconductor Science and Technology, 28, 035016 (9pp).